Contrib Mineral Petrol (1983) 84:235–252

Contributions to Mineralogy and Petrology

The white trachytic tuff of Roccamonfina Volcano (Roman Region, Italy)

Bernardino Giannetti[1] and James F. Luhr[2]

[1] Liceo Ginnasio Statale G. Carducci, 03043 Cassino (FR), Italy
[2] Department of Geology and Geophysics, University of California, Berkeley, California 94720, USA

Abstract. The White Trachytic Tuff (WTT) is a compositionally-zoned, trachytic, pyroclastic-flow deposit which erupted from Roccamonfina volcano about 300,000 years ago. It was principally emplaced as unwelded, pumice-rich flow units with an estimated volume of 10 km^3. These now cover the flanks of the volcano on all sides except the west, behind the highest rim of Roccamonfina's summit caldera; the caldera was probably in existence prior to the WTT activity.

Eruption of the WTT generally initiated the leucite-free, second stage of Roccamonfina's development, following a long history of leucite-bearing volcanism, but minor leucite-bearing lavas and pyroclastics overlie the WTT as well. The WTT was in turn followed by progressively more basic, leucite-free magmas (latite, trachybasalt, and basalt). During the course of the eruption, the WTT evolved from white, crystal-poor pumices containing 66% SiO_2 and 1.2% CaO, to grey pumices containing higher crystal contents, 60% SiO_2, and 3% CaO. Early pumices are also relatively enriched in Mn, Na, Zn, Ga, Rb, Y, Zr, Nb, Cs, La, Ce, Yb, Lu, W, Hf, Th, and U, and depleted in Ti, Fe, Mg, K, Sc, V, Cr, Co, Sr, Ba, Nd, Sm, Eu, Tb, Dy, and Ta. The pumices are essentially bimodal in composition, with several minor intermediate types including megascopic, physical mixtures of the white and grey varieties. Certain WTT pumices, including all analyzed intra-caldera samples, are relatively enriched in Pb, Th, Zr, Rb, Ga, Zn, and Cs compared to the rest of the suite. These enrichments may reflect local assimilation of carbonates or more complex exchange processes at the magma chamber margin.

All WTT pumices contain the phases sanidine, plagioclase, clinopyroxene, biotite, titanomagnetite, sphene, and apatite; grey varieties also contain magnesian olivine crystals which are probably xenocrysts. The white, crystal-poor types show relatively simple mineralogies with little compositional variability or zoning among crystals of a single phase. Other pumice types, and dark, trachyandesitic inclusions separated from white pumices, show a large compositional spectrum of individually homogeneous crystals. These compositionally diverse crystals and inclusions are interpreted as a result of widespread mixing between the trachytic magmas and more basic magmas prior to or during the WTT eruption.

Major-element crystal-fractionation models can successfully derive the early trachytes from the late trachytes by 50–85% separation of a syenitic assemblage of all phases. The predicted phase proportions and compositions closely match cumulate syenite nodules found at Roccamonfina. Trace element models are permissive of syenitic fractionation within the large uncertainties allowed by published partition coefficients.

Offprint requests to: B. Giannetti and J.F. Luhr

2 *Present address:* Department of Geology, Franklin and Marshall College, Lancaster, Pennsylvania 17604, USA

Introduction

Roccamonfina is a Pleistocene-Recent volcano, just over 1,000 m in elevation, which lies 50 km NNW of Somma-Vesuvius in the belt of potassic volcanoes along Italy's western coast (Fig. 1). It marks the intersection of two fracture systems related to post-Miocene extensional tectonism: the Appenine (NW-SE) and the Anti-Appenine (NE-SW) systems. The partially dissected strato-volcano has a present-day volume of about 100 km^3 and a base near sea-level of 17–18 km diameter. It rests on Pleistocene lacustrine sediments of the "Liri Valley" sequence (Devoto 1965), which in turn overlie Cenozoic arenites and marls, and Mesozoic limestones. Its summit is capped by a well-developed central caldera (5.5–6.5 km across) and a smaller caldera ("gli Stagli") near the northern rim of the main one (Fig. 1).

The history of Roccamonfina can be divided into two principal episodes (Giannetti 1979). The strato-volcano was primarily constructed during Stage I, from outpourings of high-K lavas and pyroclastic-fall and -flow eruptions. All Stage I products are leucite-bearing, ranging from leucite-tephrites to leucite-phonolites; they belong to the high-K series (HKS) of the Roman Region. The lavas have been dated by K-Ar in the range 1.54–0.46 million years (for a review see Giannetti et al. 1979). The last major pyroclastic-flow eruption of Stage I produced the Brown Leucitic Tuff (BLT). This formation is lacking on the western side of the volcano, behind the highest portion of the main caldera wall (Fig. 1), suggesting that the caldera was in existence or at least formed during the BLT eruption, and that its high rim acted as a barrier to flow in this direction. The strato-volcano collapse appears to have activated a series of phonolitic eruptions (+/− leucite, sodalite, and nepheline) forming lava domes and minor flows. Many of these phonolites erupted along the main caldera rim (Fig. 1), but the relative timings of collapse and phonolite eruption are still unclear.

Roccamonfina's Stage II activity was initiated some 300,000 years ago (Table 1) with eruption of the White Tra-

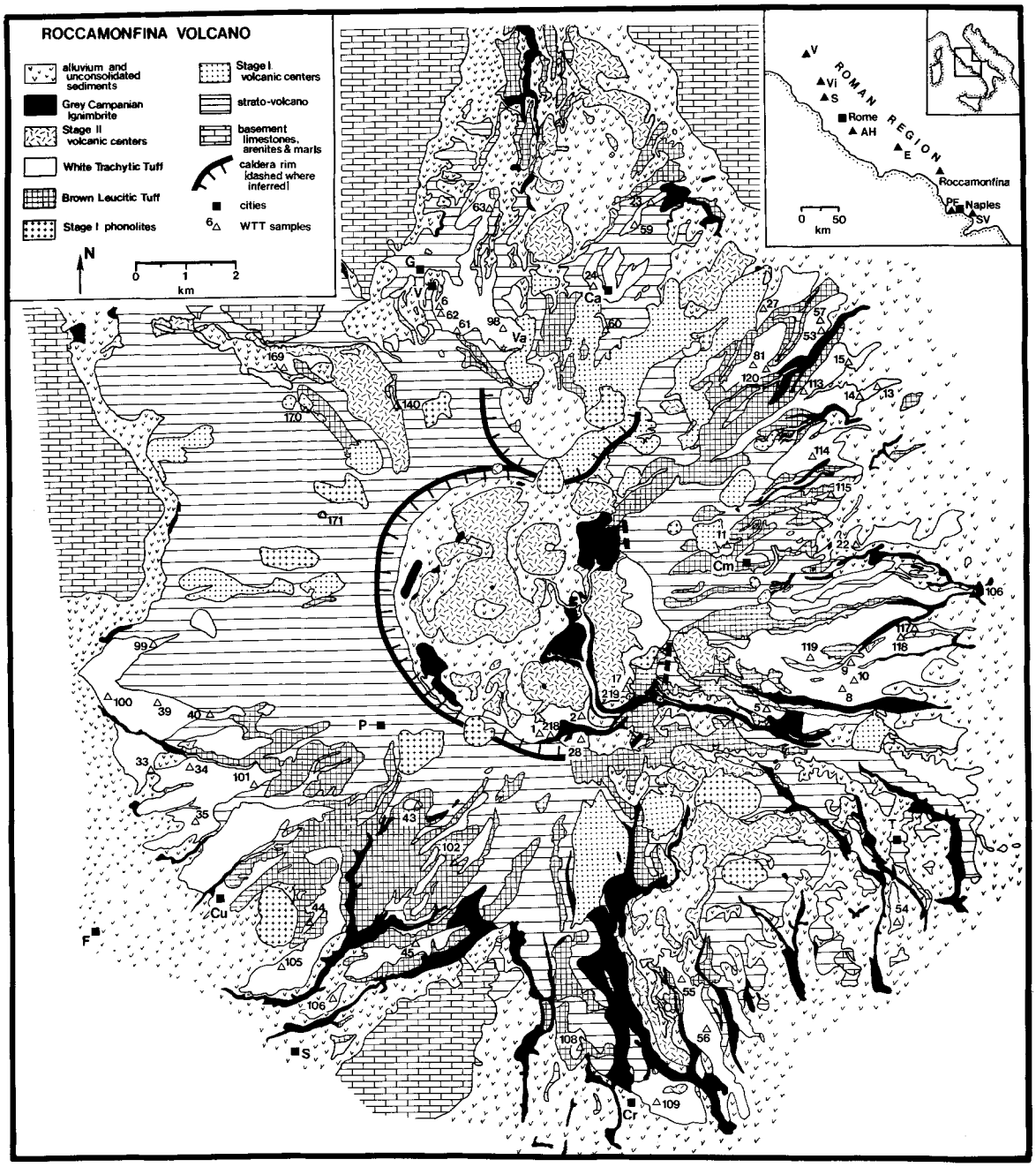

Fig. 1. Geologic map of Roccamonfina Volcano. Cities: *Ca,* Cave; *Cm,* Campagnola; *Cr,* Croce di Casale; *Cu,* Cupa; *F,* Fasani; *G,* Galluccio; *P,* Ponte; *S,* Sorbello; *T,* Teano; *V,* Volpara. Star: *Va,* Vallecuvelle field. Inset map shows western Italy and Quaternary volcanoes of the Roman Region, including: *V,* Vulsini; *Vi,* Vico; *S,* Sabatini; *AH,* Alban Hills; *E,* Ernici; *PF,* Phlegraean Fields; *SV,* Somma-Vesuvius

Table 1. K-Ar age determinations

Sample no.	Material	UCB #	Sample weight (g)	$\%K^+$	$\%^{40}Ar_{rad}$	$^{40}Ar_{rad}$ (moles/g $\times 10^{-11}$)	Age (m.y.)
35T	Sanidine	3911	5.2553	11.066	43.3	0.5898	0.307 +/− 0.004
35T	Glass	3937	4.6195	7.227	5.3	0.3802	0.303 +/− 0.024

Decay constant: $\lambda_{^{40}K_\beta} = 4.962 \times 10^{-10}$/yr; $\lambda_{^{40}K^e} + \lambda'_{^{40}K^e} = 0.581 \times 10^{-10}$/yr

Isotopic abundance: $^{40}K = 0.01167\%\ K_{total}$

Analyst: Warren Sharp

chytic Tuff (WTT), which forms the subject of this study. Subsequent eruptive activity was primarily confined to the main caldera and its margins, giving rise to a series of lava domes and minor vents with related pyroclastics. The volcanic rocks of Stage II are characterized by the absence of leucite and by relatively lower contents of K and related elements (Appleton 1972), and are referred to as the K-series (KS). They progressively changed composition with time from the WTT trachytes, through latites, to trachybasalts and basalts. Constructive activity at Roccamonfina concluded with deposition of the Grey Campanian Ignimbrite (GCI), dated at 28,000–35,000 years (Di Girolamo and Keller 1972). This voluminous trachytic ignimbrite is compositionally similar to the WTT. It apparently erupted about 50 km to the south near the Phlegraean Fields (Fig. 1; Di Girolamo 1970; Barberi et al. 1978; Cornell et al. 1979), covering a large area (>7,000 km^2) including Roccamonfina.

Appleton (1972) conducted an extensive study of lava compositions at Roccamonfina, but neglected its voluminous pyroclastic deposits. Numerous geochemical and isotopic studies based on Appleton's samples have followed in recent years (Cox et al. 1976; Carter et al. 1978; Hawkesworth and Vollmer 1979; Vollmer and Hawkesworth 1980). Ghiara et al. (1973) investigated the two principal pyroclastic-flow deposits of Roccamonfina, the BLT and WTT (called by them Units A and B respectively), giving isopleth maps and a preliminary treatment of compositional variations and mineralogy in the WTT pumices. They recognized the WTT as a pyroclastic-flow deposit and considered its eruption as responsible for the strato-volcano collapse. Later studies by Ghiara and Lirer (1977), Ghiara et al. (1979), and Vollmer et al. (1981), included WTT samples in discussions of Roccamonfina's Stage II products. Taylor et al. (1979) measured oxygen isotopic ratios in 80 Roccamonfina samples including 4 WTT specimens. These published studies have established that the transition from Stage I to Stage II magmas coincided with decreases in whole rock K, P, Ba, Ce, Nd, Rb, Sr, Th, Zr, Pb, U, and $^{87}Sr/^{86}Sr$, and increases in $^{143}Nd/^{144}Nd$ and $^{206}Pb/^{204}Pb$. Within both Stage I and Stage II suites, $^{87}Sr/^{86}Sr$, ^{18}O, $1/(^{143}Nd/^{144}Nd)$, and $1/(^{206}Pb/^{204}Pb)$ are positively correlated. The extreme values for $^{87}Sr/^{86}Sr$ (up to 0.710) and $^{143}Nd/^{144}Nd$ (down to 0.5122) at Roccamonfina have been variously explained as reflecting crustal contamination of mantle-derived magmas (Taylor et al. 1979) and metasomatism of the mantle source region (Hawkesworth and Vollmer 1979).

This paper attempts a comprehensive study of the WTT based on detailed mapping of the entire volcano. Two new K-Ar ages for the WTT are presented, as well as compositional and mineralogical data for an extensive suite of WTT pumice samples.

Field relations

The ages of Roccamonfina's two calderas and their relationship to the transition from Stage I to Stage II magmas are not firmly established. Both the WTT and the earlier BLT are distributed on all flanks of the volcano except to the west, behind the highest portion of the caldera wall (Fig. 1), indicating that the main caldera formed either prior to or during the BLT eruption. It may have been further modified during the WTT activity. The smaller northern caldera "gli Stagli" contains isolated patches of BLT (Fig. 1), similarly indicating that it formed before or during the BLT eruption.

Eruption of the WTT generally marked the transition from leucite-bearing (HKS) volcanics of Stage I to the leucite-free (KS) Stage II products, but deviations from this orderly transition have been observed; the WTT is overlain by leucite-bearing pyroclastics near Cave (Fig. 1) and by leucite-bearing lavas and pyroclastics near the field Vallecuvelle (Fig. 1). During the Stage I to Stage II transition, therefore, HKS and KS magmas were erupting alternately. Similar alternations between HKS and KS magmas characterized the life of Vulsini Volcano the the north (Varekamp 1980). The WTT forms the lowest exposed unit of the intra-caldera section, but is best seen on the outer flanks of the volcano. Intra-caldera and extra-caldera units are now discussed in turn, followed by an estimate of eruptive volume.

Intra-caldera WTT units

Within the southern portion of the main caldera, a 60-m-thick sequence of pyroclastic deposits is exposed. It begins with 15–20 m of massive WTT pyroclastic-flow units (sample 218 – Fig. 1) with an unexposed base, overlain by 5–8 m of bedded WTT ash and pumice horizons. Coarse-pumice layers in this bedded sequence are often strongly oxidized, and the upper levels usually show very fine-grained, thinly-laminated ash beds (Fig. 2). These are overlain in turn by a peculiar horizon of large (to 80 cm) WTT pumice blocks (sample 2 – Fig. 1) embedded in a matrix of thinly-laminated fine ash. The matrix laminations are often deformed and contorted around the pumice blocks. Near the southern margin of the caldera, the basal massive WTT is not present and the sequence of stratified WTT is correspondingly thicker (approximately 30 m). It includes numerous intervals of thinly-laminated fine ashes with crossbedding in coarser layers, and several repeated horizons of large pumice blocks in an ashy matrix. All sections of stratified WTT show gentle (3–5°) dips to the north and west, and are overlain by 25–30 m of subsequent Stage II pyroclastics, progressing upward from latite to trachybasalt.

The intra-caldera sequence of stratified WTT appears to have formed within a caldera lake, following the bulk of the WTT eruption. Thinly-laminated beds of fine ash represent quiet lacustrine deposition, whereas the coarser-grained layers with cross-bedding may represent saturated turbidity flows and deltaic deposition near the lake margins. The peculiar horizons containing large pumice blocks are small-scale versions of the "giant-pumice horizon" described by Mahood (1980) and Clough et al. (1981) from the Primavera Complex of Mexico. There, the extreme pumice dimensions are thought to have resulted from eruption of a lava-dome or -flow within a caldera lake, followed by detachment of large floating blocks and later gentle settling into the waterlogged, laminated fine ashes of the lake bottom.

Extra-caldera WTT units

The nature of extra-caldera WTT deposits changes markedly with distance from the caldera rim. The WTT is essentially absent on the upper part of the cone for 0.5–1.5 km from the rim (Fig. 1), implying either non-deposition or complete erosion from the steepest (10–15°) slopes of Roc-

Fig. 2. Thinly-laminated beds of fine-ash dipping gently (3–5°) to the NW, from the upper part of the intra-caldera bedded pyroclastic sequence. Stratigraphically above samples 218a and b, and below sample 2 (Fig. 1)

camonfina. Further down the flanks, WTT deposits are a few meters thick, and confined to ridge crests separated by radial ravines dissecting the volcano. Undoubtedly the WTT originally filled these ravines and has since been eroded. The ravines now expose either Stage I products or the relatively coherent BLT or "Grey Campanian Ignimbrite" (GCI) pyroclastic-flow deposits. Finally, on the basal plains surrounding Roccamonfina the outcrops become thicker and more extensive, with vertical quarry sections up to 40 m in height near Galluccio and Croce di Casale (Fig. 1). In distal exposures on the southwest flank (between Sorbello, Cupa, and Fasani – Fig. 1), WTT pyroclastic-flow units show reworking and grade upward into fluvial deposits. On the eastern and southern sides of the volcano, WTT units are also buried by alluvium.

The WTT overlies either lavas and pyroclastics of Stage I or the BLT. The latter shows up to 1 m of oxidation just below the WTT, indicating a substantial time interval between these eruptions. In other places the WTT fills clean channels cut into the BLT (e.g. near Campagnola – Fig. 1). Where the base of the WTT is exposed, it usually consists of fine-grained, thinly-laminated, milk-white ash showing planar and low-angle cross-bedding. This basal unit can be up to 1 m thick (e.g. south of Ponte – Fig. 1), and is interpreted as a ground-surge horizon, corresponding to "layer 1" of Sparks et al. (1973) and "layer a" of Fisher (1979). It grades upward through coarser stratified pumice and ash showing low-angle cross bedding, into typical white massive flow facies of the WTT. In thick quarry sections, as many as five pyroclastic-flow units can be seen, commonly separated by widespread fine ash horizons or lenses of coarse lithics. The latter may represent either lithic accumulations near the base of pyroclastic-flow units, or in other cases, mudflow deposits. No soil horizons have been seen between WTT flow units; they appear to have erupted in rapid succession. Welding is poorly developed in certain WTT outcrops on the upper slopes of Roccamonfina and within the caldera, but the massive flow units near the base of the volcano are totally unwelded. Low-angle cross-bedding is very pronounced in certain WTT units on the eastern flank (samples 10 and 22 – Fig. 1). Although the WTT is comprised primarily of pyroclastic-flow units, ash- and pumice-fall beds are also occasionally observed. The WTT eruption did not, however, begin with an early pyroclastic-fall phase, as initiates many major pyroclastic-flow eruptions (Sparks et al. 1973).

Ghiara et al. (1973) give isopleth maps of pumices and lithics within the WTT, showing that lithics are generally larger than pumices at any given outcrop. Lithics can be either dispersed throughout the ash- and pumice-rich matrix or concentrated in lenses, where they are usually rounded. Lithics range up to 1 m in diameter and include Stage I (leucite-bearing) varieties, plutonic rocks (Giannetti 1982), and calc-silicate hornfelses. Pisoliths are frequent in the WTT, reaching 3 cm in diameter in horizons east of M. Atano.

The youngest depositional unit at Roccamonfina, the GCI, rarely comes in contact with the WTT. It appears to have been restricted to radial ravines which had cut entirely through the WTT prior to GCI deposition.

Estimated volume of WTT deposits

Present outcrops of the WTT cover approximately 40 km^2 (Fig. 1); interpolation between these exposures yields a depositional area of about 250 km^2, but no exposures occur more than 8 km from the caldera rim. The original deposit was probably significantly more extensive; thick pyroclastic-flow units certainly continue beneath alluvium to the east, and others may have reached the sea to the southwest. Assuming an average thickness of 10 to 20 meters for the WTT, its present distribution implies a volume of 3–5 km^3. The primary depositional volume was probably considerably greater, in the neighborhood of 10 km^3.

Potassium argon dating

A crystal-rich, grey, WTT pumice sample (35T) was chosen for K-Ar dating at the Berkeley Lab. Nearly pure 50–150 mesh sanidine and glass fractions were concentrated by magnetic separation and heavy liquid density column. Results for these 2 samples are given in Table 1. The sanidine and glass ages are indistinguishable within the reported uncertainties. The sanidine gave a high yield of radiogenic

Table 2. XRF Analyses of whole-rock and glass samples

	6wr	43wr	35Bwr	11wr	35Twr	13wr	6gl	43gl	35Bgl	11gl	35Tgl	13gl	99inc	100inc
(wt.%)														
SiO_2	65.47	59.75	64.14	60.70	60.96	60.55	65.80	59.60	64.66	61.34	61.54	61.56	56.35	57.00
TiO_2	0.23	0.16	0.29	0.41	0.49	0.52	0.22	0.15	0.26	0.39	0.48	0.49	0.67	0.63
Al_2O_3	18.49	22.41	18.65	20.33	19.19	19.07	18.62	22.64	18.52	20.56	19.16	19.25	19.67	18.86
FeOt	2.14	2.13	2.38	2.67	3.00	3.19	2.13	2.06	2.23	2.34	2.81	2.86	4.74	4.63
MnO	0.21	0.17	0.19	0.09	0.11	0.11	0.21	0.17	0.19	0.09	0.12	0.12	0.11	0.10
MgO	0.29	0.19	0.43	0.52	0.73	1.10	0.24	0.24	0.14	0.32	0.48	0.50	2.59	2.85
CaO	1.20	1.45	1.56	2.52	2.80	3.15	1.13	1.33	1.32	2.02	2.25	2.26	5.52	5.53
Na_2O	4.98	6.16	5.21	3.85	3.86	3.68	4.74	6.47	5.69	4.16	4.16	4.14	2.90	2.78
K_2O	6.88	7.46	7.05	8.78	8.74	8.52	6.79	7.23	6.87	8.66	8.89	8.72	7.22	7.40
P_2O_5	<d.l.	<d.l.	<d.l.	<d.l.	<d.l.	<d.l.	<d.l.	<d.l.	<d.l.	<d.l.	<d.l.	<d.l.	0.20	0.20
Total	100.00	100.00	100.00	100.00	100.00	100.00	100.00	100.00	100.00	100.00	100.00	100.00	100.00	100.00
(ppm)														
V	<d.l.	<d.l.	13	48	62	79	12	<d.l.	17	27	51	46	132	147
Cr	<d.l.	<d.l.	<d.l.	<d.l.	<d.l.	<d.l.	<d.l.	<d.l.	<d.l.	<d.l.	<d.l.	<d.l.	61	71
Pb	85	132	68	64	48	45	85	138	86	78	51	42	48	36
Th	76	87	71	55	26	28	76	87	73	66	33	30	34	24
Rb	582	710	521	461	318	340	608	739	555	472	340	349	286	275
Sr	32	52	148	657	713	721	27	28	94	450	595	566	1,037	1,480
Y	57	36	55	55	45	50	56	33	53	42	49	44	30	36
Zr	672	924	594	375	271	277	699	951	624	397	290	291	187	194
Nb	39	51	37	40	25	25	40	53	41	37	28	29	53	20
Ni	13	<d.l.	<d.l.	10	16	22	14	12	29	10	15	9	14	39
Cu	35	43	9	30	16	56	18	12	21	28	10	20	18	83
Zn	109	116	98	67	60	74	104	107	108	68	57	60	71	82
Ga	24	38	25	17	19	16	32	34	27	17	16	20	23	15
Cs	17	31	13	10	6	9	20	31	14	8	8	7	2	4
Ba	<d.l.	<d.l.	83	189	387	376	14	12	66	104	343	310	844	1,046
La	168	133	150	134	90	102	168	129	163	142	115	83	70	55
Ce	227	168	208	202	185	164	230	164	240	205	185	164	96	102
P.T.	I	I	III	IV	II	II								
crystals	f	f	f	a	m	m								
inclusions	n	f	a	f	m	m								

wr = whole rock, gl = glass
d.l. = detection limit: P_2O_5 (0.11%), V (3 ppm), Cr (3 ppm), Ni (7 ppm), Ba (6 ppm)
Counting uncertainties of one standard deviation are: V (5%), Cr (5%), Pb (7%), Th (7%), Rb (5%), Sr (5%), Y (15%), Zr (5%), Nb (15%), Ni (15%), Cu (12%), Zn (8%), Ga (10%), Cs (15%), Ba (3%), La (10%), and Ce (10%) of the amounts present
Trace element concentrations not normalized to 100%
Crystals and inclusions indicate amounts estimated in hand specimen: n = none, f = few, m = moderate, a = abundant
P.T. = pumice type: I) white with few – moderate crystals II) grey and crystal-rich III) white with abundant grey inclusions IV) white and feldspar-rich
inc – dark inclusion from white-pumice host

^{40}Ar (43%), and its age of 307,000 +/− 4,000 years is preferred. Cortini et al. (1975) published a less precise K-Ar age on WTT sanidine of 0.25 +/−0.04 m.y. (26% Ar_{rad}), which does not overlap with our determined age within the reported uncertainties. Similarly, Cortini et al. (1975) reported four ages determined on Stage I lavas of Roccamonfina (0.46–0.56 m.y.; >20% Ar_{rad}) which are significantly younger than ten ages determined by Giannetti et al. (1979) on other Stage I lavas (0.71–1.54 m.y.; >20% Ar_{rad}).

Whole rock and glass compositions

Visual observations

The WTT is an unwelded pumice-rich pyroclastic-flow deposit, consisting of ash, pumice, crystals, and lithics. Sanidine, clinopyroxene, biotite, and plagioclase, all under 1 mm in size, are the main crystals of the matrix. Strongly altered leucite crystals can be very abundant in the matrix, but are definitely lithic-derived, as they are absent in the WTT pumices. Cryptocrystalline chabazite is always present as a matrix phase. 69 pumice samples were collected from the WTT at locations indicated on Fig. 1. Pumice clasts are generally less than 15 cm in diameter, but range up to 80 cm in the large-pumice horizons capping the intracaldera WTT. Vesicles show no indication of flattening, even in the basal flow units. The pumices can be broadly divided into four groups on the basis of megascopic properties: I) white with few – moderate crystals (41 samples), II) grey and crystal-rich, including both dense and vesicular varieties (20), III) white pumices with abundant, cm-sized grey inclusions (5), and IV) white pumices with abundant feldspar phenocrysts (3). An attempt was made to visually estimate the percentage of both crystals and inclusions in

Table 3. Instrumental-neutron-activation analyses of WTT pumices

Sample	6		43		35T	
PT	I		I		II	
Na%	3.88	(0.08)	4.69	(0.09)	2.85	(0.06)
Al%	8.83	(0.14)	10.7	(0.2)	9.32	(0.16)
Sc	0.44	(0.01)	0.16	(0.01)	4.04	(0.03)
Ti%	0.13	(0.01)	<0.05		0.25	(0.02)
Cr	3.3	(0.7)	2.2	(0.9)	19.7	(0.7)
Mn	1,551	(30)	1,213	(24)	926	(18)
Fe%	1.28	(0.02)	1.18	(0.02)	2.07	(0.03)
Co	1.22	(0.08)	0.89	(0.09)	3.83	(0.12)
Ni	<8		<8		<10	
Zn	117	(3)	110	(3)	81	(4)
Rb	601	(19)	710	(23)	363	(12)
Cs	68	(1)	115	(2)	25.2	(0.4)
Ba	<49		<38		330	(17)
La	154	(2)	122	(2)	92	(1)
Ce	266	(4)	182	(3)	182	(3)
Nd	50	(3)	23	(3)	72	(3)
Sm	7.11	(0.02)	3.18	(0.02)	12.39	(0.02)
Eu	0.80	(0.01)	0.43	(0.01)	2.96	(0.02)
Tb	0.73	(0.03)	0.25	(0.03)	1.84	(0.03)
Dy	5.74	(0.21)	2.59	(0.20)	7.25	(0.19)
Yb	5.34	(0.11)	3.24	(0.09)	3.30	(0.08)
Lu	0.71	(0.03)	0.53	(0.02)	0.40	(0.02)
Hf	15.2	(0.2)	17.1	(0.3)	6.7	(0.1)
Ta	1.35	(0.01)	1.33	(0.01)	1.57	(0.01)
W	13.8	(1.0)	6.9	(0.8)	5.0	(0.6)
Th	75.3	(0.3)	82.5	(0.3)	28.2	(0.1)
U	17.0	(0.1)	30.2	(0.2)	5.89	(0.05)

INA analyses by F. Asaro and H. Michel, Lawrence Berkeley Laboratory (Perlman and Asaro 1969). Data in ppm except for Na, Al, Ti, and Fe (wt%). Numbers in parentheses are one standard deviation counting uncertainties
The samples were ground in agate to avoid W-Co-Ta contamination
P.T. = pumice type as in Table 2

each pumice sample, categorizing them as: "n" – none, "f" – few, "m" – moderate, and "a" – abundant. These parameters and pumice-type groupings are listed for each sample in Table 2 and Appendix 1. The four major pumice types are designated by different symbols on following compositional plots. In addition to the pumice samples, two dense, dark inclusions, 5–10 cm in diameter, were separated from white pumice hosts for analysis.

Analytical techniques

The 69 pumice samples and 2 dark inclusions were oven-dried and cleaned by nylon brush and compressed air. They were then crushed in a tungsten carbide mortar and ground for 15 min in an acetone slurry using a SPEX shatterbox, also of tungsten carbide. After drying, powders were pressed into aluminium cups at 20,000 psi. These undiluted pressed powder pellets were analyzed on a United Scientific energy-dispersive x-ray-fluorescence machine for 10 major and 17 trace elements. The method of XRF major element analysis depends upon well analyzed, compositionally similar standards. For this purpose, five WTT samples were wet chemically analyzed following Falchi and Tonani (1962). A least-squares fit of each analyzed spectrum into the 10 major elements of interest gave counts for each element. The five standards were used to calibrate linear equations of counts vs. concentration for each element, which were then applied to the unknowns. The standards analyzed in this study and the white and grey WTT pumice analyses reported by Ghiara and Lirer (1973) yield 2–6 wt.% H_2O^- plus loss on ignition, and for this reason, all major-element analyses are normalized to 100% anhydrous. Uncertainties of one standard deviation calculated from analysis of additional trachytic pumice standards correspond to the following absolute amounts: SiO_2 (1%), TiO_2 (0.05%), Al_2O_3 (0.7%), FeO' (0.1%), MnO (0.05%), MgO (0.05%), CaO (0.05%), Na_2O (0.5%), K_2O (0.1%), P_2O_5 (0.03%).

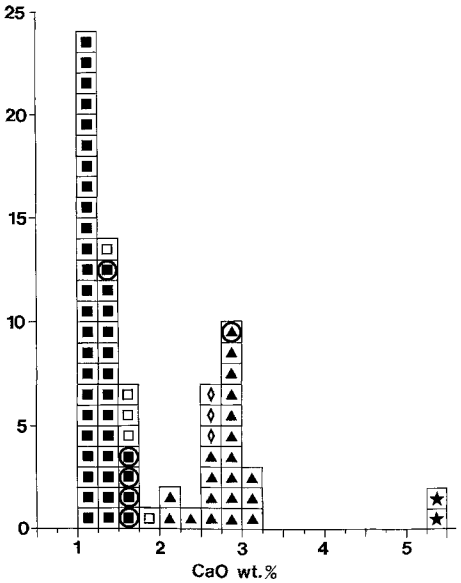

Fig. 3. Histogram of CaO contents in 69 WTT pumice samples and two dark inclusions with different symbols representing different pumice types: closed squares (Type I) white with few-moderate crystals; triangles (Type II) grey and crystal-rich; open squares (Type III) white with abundant grey inclusions; open diamonds (Type IV) white and feldspar-rich; stars – dark inclusions 99inc and 100inc separated from white-pumice hosts; large circles surround symbols for six intra-caldera samples

Of the 71 analyzed specimens, six representative samples were chosen for determination of modes and mineral and glass analyses. These samples range across the compositional spectrum and represent the four major megascopic groups discussed above: samples 6 and 43 – Pumice Type I, samples 35T and 13 – Type II, sample 35B – Type III, sample 11 – Type IV. Whole-rock and glass analyses of these six samples and the two dark inclusions are listed in Table 2. Also indicated are pumice type and crystal and inclusion contents. Three of the six samples, 6, 43, and 35T, were also analyzed by INA. Results and uncertainties are given in Table 3. The remaining 63 pumice analyses are available upon request.

Compositional variations among WTT pumices

In this study we use CaO as the principal compositional index variable because: 1) it shows a wide variation in the WTT suite (1–5.5 wt.%), 2) it correlates strongly with most other elements, 3) XRF precision for CaO is relatively high, and 4) CaO has traditionally been chosen as an index variable for Italy's potassic igneous rocks (Appleton 1972; Giannetti 1982). Figure 3 shows a histogram of CaO contents for the 71 WTT samples, with different symbols representing the four megascopic pumice types and the dark inclusions. The WTT is clearly bimodal compositionally. The dominant peak (1–2% CaO) includes Type I white pumices, and the 5 white pumices with abundant dark inclusions (Type III), which fall on the more calcic side of the peak. The other major peak (2–3.5% CaO) is dominated by grey (Type II) pumices, with the 3 white and feldspar-rich samples (Type IV) on the less calcic side of the peak.

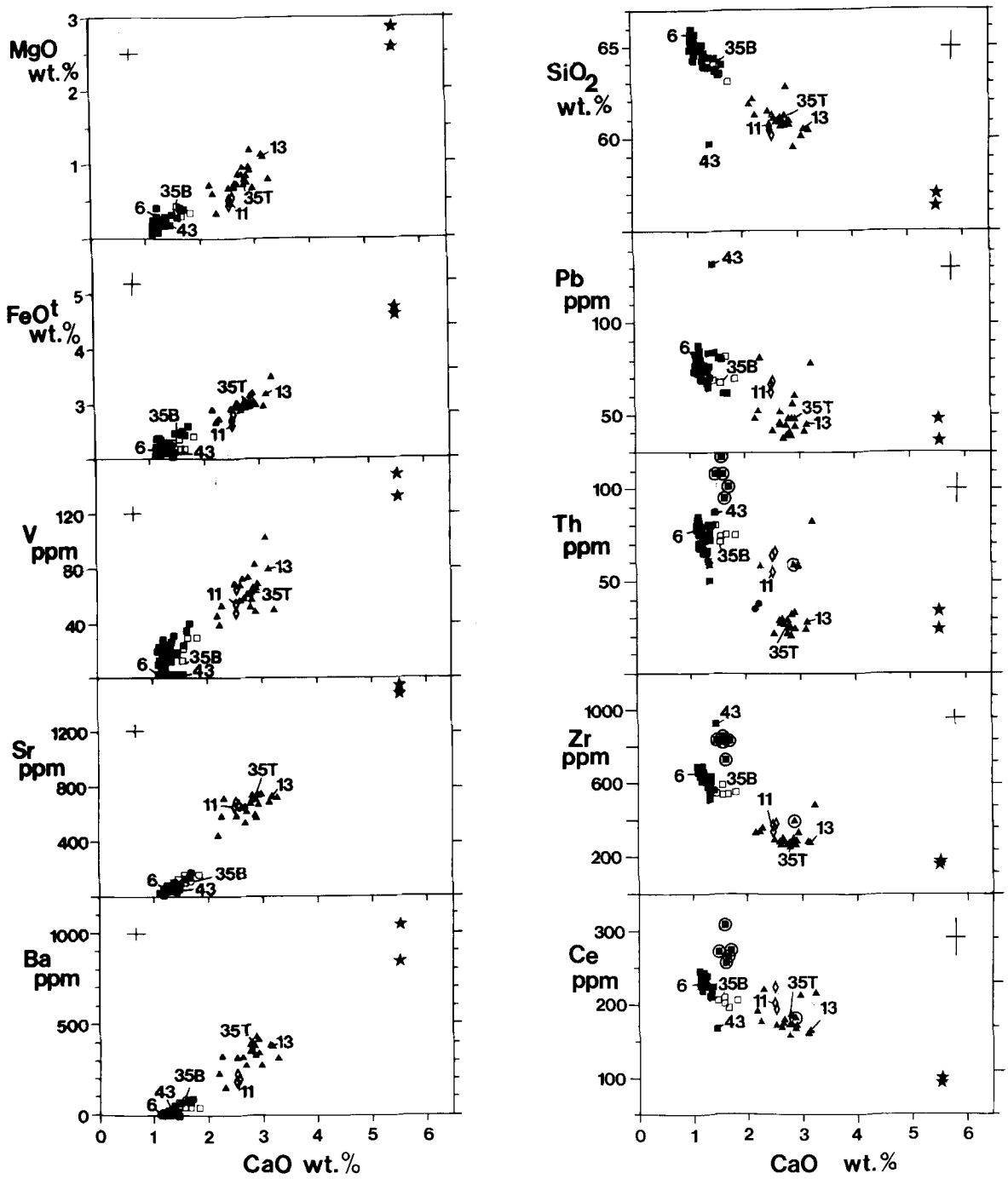

Fig. 4. Compositional variations among WTT samples. Different symbols represent different pumice types and dark inclusions as in Fig. 3. Error crosses indicate 1 std. dev. uncertainties

The two separated inclusions, with 5.5% CaO, are significantly more basic than any pumices.

Six intra-caldera WTT samples are distinguished by large circles around their respective symbols. Five of these are nearly identical in composition with about 1.5% CaO. Sample 2, from the large-pumice horizon which caps the intra-caldera WTT, is considerably more calcic (2.9% CaO).

Figure 4 shows selected variation diagrams of whole-rock WTT samples, again using CaO as an index variable. The four pumice types and the inclusions are distinguished by the same symbols as in Fig. 3. As CaO decreases amongst the WTT samples, SiO_2, MnO, Na_2O, Zn, Ga, Rb, Y, Zr, Nb, Cs, La, Ce, Yb, Lu, Hf, W, Th, and U increase, while TiO_2, FeO^t, MgO, K_2O, Sc, V, Cr, Co, Sr, Ba, Sm, Eu, Dy, and Ta decrease. On all plots, the majority of the samples fall within two elongate clusters, corresponding to the main peaks on Fig. 3, Pumice Types I (closed squares) and II (triangles). The inclusion-rich white pumices (Type III – open squares) plot between these two clusters adjacent to Type I pumices, consistent with their interpretation as a mixture of Type I trachyte and a more basic end-member. Five elements which increase with CaO are plotted on the left side of Fig. 4, showing strong correla-

tions with few deviate points. The two analyzed dark inclusions (Table 2) plot along trend-lines extrapolated from the WTT pumices to more basic (CaO-rich) compositions. They appear to be transitional between the WTT trachytes and the younger, Stage II latites, and are hereafter referred to as trachyandesites. Five elements which increase with decreasing CaO, plotted on the right side of Fig. 4, show much greater scatter, well beyond deviations attributable to analytical uncertainty (1σ uncertainties are shown by error crosses). Again, most samples conform to the two principal clusters. Certain pumices, including all intra-caldera samples (circled), deviate markedly from the main trends. They are relatively enriched in Pb, Th, Zr, Rb, Ga, Zn, and Cs. Sample 43 is the most extreme case; it alone is relatively poor in SiO_2 and strongly ne-normative. The INA data in Table 3 show further that 43 is relatively enriched in Hf and U, and uniformly depleted in REE's compared to Type I sample 6. As discussed in the next section, this sample is also unique in containing andradite-grossular garnet and hastingsitic amphibole. These enriched samples have a wide range of CaO contents and include most major pumice types. They principally occur within the caldera or on the high southern flank (43 – Fig. 1). These relative enrichments are discussed further in a later section.

Figure 5 is a chondrite normalized REE plot for the three WTT samples listed in Table 3. The relatively calcic Type II pumice sample 35T shows a nearly linear, LREE-enriched pattern. Type I pumice sample 6 contains relatively higher contents of La, Ce, Yb, and Lu, but shows depletion of the middle REE's, particularly Eu. The pattern for sample 43 mimics that for sample 6 at lower values.

Compositional variations in time and space

The two dominant compositional groups of the WTT are easily distinguished in the field by their respective white and grey pumices. Single WTT outcrops are dominated either by white or grey pumices, although careful searching yields a few grey-pumice fragments in outcrops of white and vice-versa. Several outcrops, particularly on the SW side of the volcano, show basal white-pumice flow units overlain by grey-pumice units, clearly establishing that the more basic (CaO and MgO-rich) grey pumices generally followed the white in order of eruption. To test for such variations in eruptive composition with time on a finer scale, eight thick exposures of WTT showing one or more flow units were sampled at the base and top; the concentrations of selected elements from these top-bottom pairs are listed in Table 4. Each pair has the same sample number followed by T for the top sample and B for the bottom sample. Four of the pairs have grey (Type II) pumices overlying white pumices (Types I and III). The other four pairs involve only white (Type I) pumices. Two of the latter samples, 22B and T, are nearly identical in composition, but the other seven sample pairs show subtle to strong trends to more basic compositions with time, with the top samples enriched in MgO, CaO, Sr, and Ba, and depleted in Rb and Zr. This appears to be the general trend for compositional variations in the WTT with time. The earliest pyroclastic flows of the WTT eruption (1.1–1.3% CaO) moved principally to the NE and E. Intermediate and late-stage flows (>1.3% CaO) moved in all directions, but primarily to the NE and SW. Six analyzed intra-caldera pumices contain 1.5–2.9% CaO; none correspond to the earliest eruptive phase (1.1–1.3% CaO), but such early pumices may underlie the deepest accessible intra-caldera levels.

Table 4. Compositional variations in stratigraphically-related sample pairs

Sample	P.T.	(wt.%)		(ppm)			
		MgO	CaO	Rb	Sr	Zr	Ba
9T	I	0.23	1.21	528	58	615	21
9B	I	0.17	1.18	544	37	663	20
10T	I	0.59	1.23	568	78	660	25
10B	I	0.15	1.14	595	32	676	12
15T	II	0.59	2.24	382	592	341	327
15B	I	0.21	1.26	534	52	616	27
22T	I	0.15	1.19	622	29	694	d.l.
22B	I	0.15	1.13	591	23	690	d.l.
27T	II	0.70	2.63	342	659	266	323
27B	I	0.08	1.22	572	32	655	23
35T	II	0.73	2.80	318	713	271	387
35B	III	0.43	1.56	521	148	594	83
57T	I	0.29	1.36	518	81	553	48
57B	I	0.18	1.17	578	25	665	13
117T	II	0.71	2.18	407	459	331	236
117B	I	0.17	1.21	611	52	667	10

T = top of outcrop; B = base of outcrop
Data from Table 2 and Appendix 1
P.T. = pumice type as in Table 2

Mineralogy

White pumices from the WTT generally contain few crystals, and the conventional technique of thin section point counting is, therefore, unreliable for determining quantitative modes. Wt.% modes were calculated for the six samples in Table 2 using a method of quantitative heavy-liquid mineral separation modified after Lipman (1967). The results are listed in Table 5. For comparison, the grey, crystal-rich pumice sample 35T (Type II) was point counted in the conventional manner and the mode converted to wt.% using appropriate densities. The two methods compare favorably for this relatively dense pumice. All samples contain sanidine, plagioclase, clinopyroxene, biotite, titanomagnetite, sphene, and traces of apatite. Sample 11 (Type IV) is characterized by relatively high contents of plagioclase and particularly sanidine. The compositionally-anomalous sample 43 (Type I) is notable for its low total crystal content and the unique presence of hastingsitic amphibole and garnet. Samples 35T, 13 (Type II), and 35B (Type III) also contain magnesian olivine. Total crystal content ranges from 1.6 wt.% in sample 43, to 15.7 wt.% in the feldspar-rich sample 11.

Grain sizes are similar in the three white, crystal-poor pumices (6, 35B, 43): sanidine to 0.5 mm, clinopyroxene to 0.4 mm, plagioclase, titanomagnetite, and biotite to 0.3 mm, sphene to 0.2 mm. Minerals are larger in the crystal-rich white-pumice sample 11: sanidine to 8 mm, plagioclase to 1 mm, clinopyroxene and biotite to 0.7 mm. Crystals are larger still in the grey pumices (35T and 13) and

Table 5. Modes

Sample	Heavy liquid separation (wt.%)						point count (wt.%)	
	6	43	35B	11	35T	13	35T	35T-inclusion
P.T.	I	I	III	IV	II	II	II	–
Sanidine	3.4	1.2	4.2	11.4	5.4	5.0	5.0	2.4
Plagioclase	0.5	0.2	0.6	3.2	1.7	1.5	3.0	3.6
Clinopyroxene	0.1	0.1	0.5	0.4	1.5	2.2	0.5	1.0
Biotite	0.001	0.01	0.05	0.09	0.2	0.1	0.3	0.2
Titanomagnetite	0.07	0.05	0.1	0.6	0.3	0.3	0.5	tr
Olivine	–	–	0.01	–	0.03	0.2	–	–
Amphibole	tr	0.02	–	–	–	–	–	–
Garnet	–	0.01	–	–	–	–	–	–
Sphene	0.03	0.01	0.06	0.04	<0.01	0.005	–	–
Apatite	tr	tr	tr	tr	0.01	tr	tr	–
Glass	95.9	98.4	94.5	84.3	90.8	90.7	90.7	92.9
Sum Crystals	4.2	1.6	5.4	15.7	9.2	9.3	9.3	7.1

Method of modal analysis described in Appendix 2, available upon request
P.T. = pumice type as in Table 2

in dark inclusions: feldspars to 5 mm, and megacrysts of clinopyroxene and biotite up to 1.5 cm and 7 cm long, respectively.

The matrices of white-pumice samples 6, 43, 35B, and 11 are vesiculated, white glass, with perhaps 1% crystallites. The more basic grey-pumice samples 35T and 13 are much less vesicular, and their brownish matrices show nearly 50% crystallites. Sharply bounded regions of differing matrix crystallinity are present in single thin sections. Dark inclusions from all pumice types look little different from the grey pumices in thin section: slightly vesiculated microcrystalline groundmasses enclosing sanidine, plagioclase, clinopyroxene, biotite, and titanomagnetite. A large (5 cm) inclusion was separated from sample 35T and point counted. It is similar to the dark inclusions (Table 2) plotted on Figs. 3 and 4. Its mode (Table 5) is little different than that of the grey-pumice host. The inclusion matrices are often more coarsely crystalline than the grey pumices, also showing sharply bounded textural domains within one inclusion. The percentage of inclusions in various samples is very difficult to estimate. Sample 6 and most other Type I pumices appear to be inclusion-free. During modal analysis, 5 wt.% of cm-sized inclusions were separated from sample 35B; perhaps 5–10% more were too small to separate. The percentage of inclusions is particularly difficult to estimate in the grey pumices, where the inclusions and pumices are similar in color. Many WTT pumices show sanidine-rich crystal clusters enclosed within and lining the walls of large vesicles. These clusters are discussed further below.

An early attempt to investigate mineral compositions in 30 WTT pumices revealed extreme compositional variability for most mineral groups, reflected in numerous compositional subpopulations in single pumice fragments. In order to determine the origin of these subpopulations, a variety of microprobe mounts were prepared for the six selected samples. Dark inclusions were observed and separated from all samples except #6. Large crystals encountered during crushing for modal analysis were similarly separated. For all samples, the crystals separated from single pumice fragments during modal analysis and sanidine-dominated crystal clusters from large vesicles were also studied. These three groups, crystal separates, large crystals, and inclusions, were embedded in epoxy and thin sectioned for probe study. For the more crystal-rich samples 11, 35T, and 13, whole-rock chips were also impregnated and thin sectioned as probe mounts. In this way we attempted to identify compositional populations with particular textural groupings. Mineral compositions in the six studied pumices are described below. Sample 6, representing the dominant, Type I pumices, has the simplest mineralogy, whereas the inclusion-rich white pumices (Type III), and the grey pumices (Type II) contain numerous compositional subpopulations of each phase.

Microprobe techniques

All minerals were analyzed on the Berkeley 8-channel ARL microprobe at 15 Kv accelerating potential using a focused electron beam approximately 1 μm in diameter. Minerals of similar composition to the unknowns were used as standards. Sample currents were 30 nA for olivine, titanomagnetite, clinopyroxene, sphene, garnet, and amphibole, and 10 nA for biotite and feldspars. In analyzing Y, Nb, and rare-earth elements in sphenes and garnet, Nb metal and the synthetic glasses of Drake and Weill (1972) were used as standards. $L\alpha_1$ peaks were used for Y and La, while $L\beta_1$ peaks were used for Ce, Nd, and Gd.

Feldspars

Both sanidine and plagioclase are present in all WTT pumices. The simplest case is that of Type I pumice sample 6, which is white and inclusion-free, and contains a single population of euhedral, inclusion-free sodic sanidine (Or_{51}), and a single population of euhedral, inclusion-free sodic plagioclase (An_{16}). These analyses are listed in Table 6 and plotted on Fig. 6. In the white, inclusion-rich (Type III) sample 35B, the dominant feldspar populations are identical to those in sample 6, but subordinate populations of K-sanidine (Or_{84}) and Ca-plagioclase (An_{87} – usually inclusion riddled) are present in bulk mineral separates (Fig. 6). Feldspars in the inclusions of 35B are exclusively K-sani-

Table 6. Average microprobe analyses of feldspar compositional subpopulations

Sample	6-s	6-p	43-s	43-p	35T-s	35T-p	35T-s	35T-p
P.T.	I	I	I	I	II	II	II	II
Analysis	a	b	c	d	e	f	g	h
SiO_2	66.24	64.18	65.39	58.87	64.66	45.69	64.85	53.92
Al_2O_3	19.48	22.18	19.28	25.42	19.08	34.11	19.37	28.62
FeO	0.23	0.30	0.16	0.32	0.20	0.64	0.31	0.50
BaO	0.00	0.00	0.00	0.00	0.09	0.01	0.02	0.00
SrO	0.10	0.12	0.13	0.17	0.25	0.86	0.15	0.25
CaO	0.56	3.47	0.45	7.52	0.40	17.54	1.00	11.36
Na_2O	5.27	8.43	3.86	6.77	1.61	1.30	3.49	4.70
K_2O	8.70	2.06	10.67	1.22	13.94	0.25	10.86	1.09
Total	100.58	100.74	99.94	100.29	100.23	100.40	100.05	100.44
X_{Ca}	0.027	0.164	0.022	0.354	0.020	0.868	0.050	0.537
X_{Na}	0.466	0.721	0.347	0.577	0.146	0.117	0.312	0.402
X_K	0.507	0.116	0.631	0.069	0.834	0.015	0.639	0.061

s = sanidine; p = plagioclase; Small letters a–h correspond to analyses plotted on Fig. 6
P.T. = pumice type as in Table 2

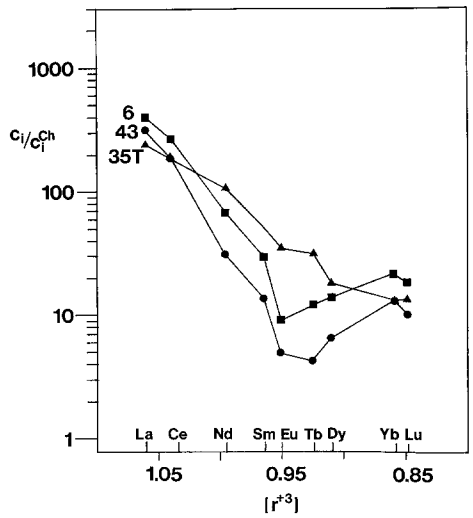

Fig. 5. Chondrite-normalized REE plot referenced to the Leedy chondrite (Masuda et al. 1973) for WTT whole-rock samples 6, 43, and 35T from Table 3

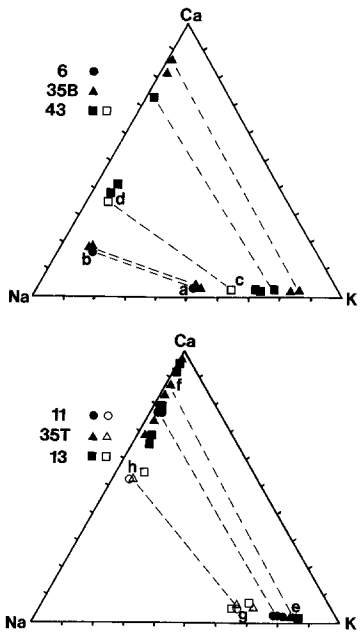

Fig. 6. Ternary feldspar diagrams (mol%) showing analyses of feldspar subpopulations in six WTT samples. Closed symbols represent core analyses or homogeneous crystals. Open symbols show rim analyses. Dashed lines indicate equilibrium pairs. Small letters a–h correspond to feldspar analyses in Table 6

dine and Ca-plagioclase, and dissolution or disaggregation of such inclusions is undoubtedly responsible for the presence of these subpopulations in the bulk feldspar separate. In the compositionally-anomalous (Type I) sample 43, two feldspar subpopulations exist (Fig. 6), with the more Na-rich sanidine (Or_{63}) and plagioclase (An_{35}) generally rimming more K-rich (Or_{77}) and Ca-rich (An_{73}) cores, respectively. Thin (0.03 mm) rims of Na-sanidine on plagioclase cores are also common. Analyses of the rim compositions are given in Table 6. The feldspar-rich (Type IV) sample 11 contains euhedral sanidine crystals up to 8 mm in diameter. Both sanidine (Or_{78}) and plagioclase (An_{77}) have broadly homogeneous cores with more sodic rims (Or_{57}, An_{52} – Fig. 6). The two grey (Type II) samples 35T and 13 are nearly identical compositionally and mineralogically. Again, K-rich sanidine cores (Or_{84}) are rimmed by more sodic sanidine (up to Or_{64}), and Ca-plagioclase cores (An_{87}) also have more sodic rims (An_{54}; Fig. 6). Rim-core analyses for feldspars of 35T are listed in Table 6. The dark inclusions separated from these 2 grey-pumice samples contain feldspars similar in composition to the phenocryst cores, but also including some very calcic plagioclases (An_{92-96}; Fig. 6). Such calcic plagioclases also occur as inclusions in clinopyroxenes. Feldspars separated from sanidine-dominated crystal clusters in vesicles are similar in composition to phenocrysts.

Clinopyroxene

As is true in many of Italy's high-K volcanics, the compositional complexity of clinopyroxenes in the WTT pumices is easily appreciated in thin section. Individually homogeneous crystals with a wide range of Fe/Mg ratios are present

Table 7. Average microprobe analyses of selected clinopyroxene and olivine subpopulations

Sample	6-cp	43-cp	35B-cp	35B-cp	11-cp	35T-cp	13-cp	35B-ol	13-ol
P.T.	I	I	III	III	IV	IV	II	III	II
Analysis	a	b	c	d	e	f	g	h	i
SiO_2	51.18	44.47	50.85	49.63	47.60	47.45	47.96	41.09	39.81
TiO_2	0.31	1.41	0.35	0.53	1.08	1.19	0.96	0.00	0.00
Al_2O_3	1.76	7.75	2.06	2.79	5.95	6.23	5.44	0.00	0.00
FeO	11.98	15.36	11.99	13.09	10.97	10.23	10.17	10.33	14.68
MnO	1.46	0.64	1.40	1.53	0.33	0.31	0.38	0.17	0.20
MgO	10.11	7.21	10.13	9.15	10.54	11.24	11.30	48.72	44.25
CaO	22.12	22.14	22.01	21.65	23.03	23.22	23.08	0.33	0.29
Na_2O	1.06	0.99	1.13	1.19	0.65	0.44	0.56	0.00	0.00
Total	99.97	99.67	99.93	99.56	100.15	100.32	99.84	100.64	99.23
X_{Fe}	0.205	0.272	0.206	0.229	0.185	0.171	0.170	0.106	0.156
X_{Mg}	0.309	0.227	0.310	0.285	0.317	0.334	0.336	0.890	0.840
X_{Ca}	0.486	0.501	0.484	0.486	0.498	0.496	0.494	0.004	0.004

cp = clinopyroxene, ol = olivine; Letters a–i correspond to analyses plotted on Fig. 7
Analyses c–d represent a rim-core pair from 35B; P.T. = pumice type as in Table 2

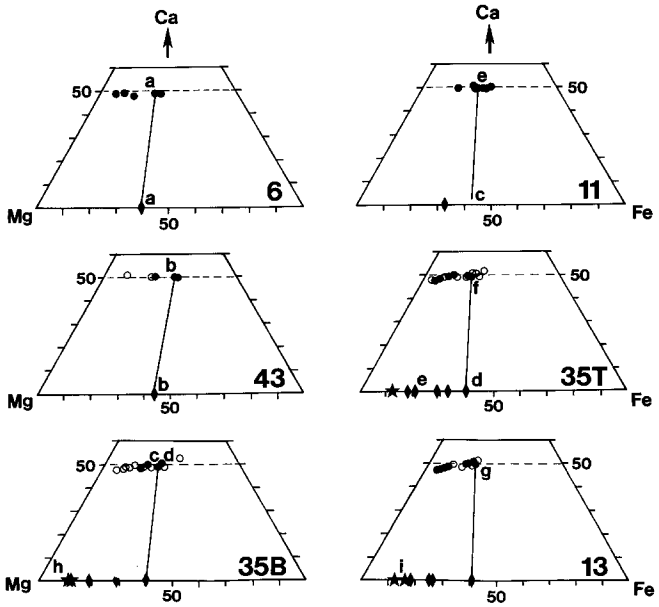

Fig. 7. Analyses of clinopyroxene (circles), biotite (diamonds), and olivine (stars) subpopulations from WTT samples plotted in the pyroxene quadrilateral (mol%). For pyroxenes, solid circles are crystals from bulk mafic separates and open circles show crystals from separated dark inclusions. Deduced clinopyroxene-biotite tie lines are indicated for the dominant subpopulations in each sample. Small letters a–i correspond to analyses in Tables 7 and 8

in single samples; Mg-rich diopside crystals are pale green under the microscope, while Fe-rich salite crystals are dark green. Although single crystals in the WTT are generally homogeneous, complex color (Fe/Mg) banding is occasionally observed.

In sample 6 (Type I), the dominant clinopyroxene population is relatively Fe-rich salite with slight Mg-rich rims. The average rim analysis ($X_{Mg} = Mg/Mg + Fe^{+2} + Ca = 0.29$) is given in Table 7. Averaged subpopulation analyses for all samples are plotted in Fig. 7. Isolated crystals with considerably higher Mg contents (to $X_{Mg} = 0.45$) are also present in the bulk mineral separate. In bulk mineral separates from sample 43 (Type I), 2 populations of homogeneous salite crystals are present ($X_{Mg} = 0.31$ and 0.23). Clinopyroxenes from separated dark inclusions, shown by open circles on Fig. 7, correspond to the relatively Mg-rich population, with one more-magnesian core ($X_{Mg} = 0.40$; Fig. 7). One of the Fe-rich salite analyses is given in Table 7 (b). In the inclusion-rich sample 35B (Type III), the dominant clinopyroxene population has slightly Mg-rich rims ($X_{Mg} = 0.31$) on more Fe-rich cores ($X_{Mg} = 0.29$) similar to the dominant clinopyroxene population in sample 6. Rim-core analyses are given as "c" and "d" in Table 7. Other more Mg-rich, homogeneous crystals are present in the mafic separate. In the inclusions of 35B (open circles), many different populations of essentially homogeneous, Mg-rich crystals are observed (up to $X_{Mg} = 0.47$). Several isolated salite crystals are also present in the inclusions ($X_{Mg} = 0.21$). In the feldspar-rich sample 11 (Type IV), most clinopyroxene rims are homogeneous ($X_{Mg} = 0.32$) while cores can be either more Fe-rich ($X_{Mg} = 0.25$) or more Mg-rich ($X_{Mg} = 0.38$). The average rim composition is given in Table 7 (e). The grey (Type II) samples 35T and 13 both show wide ranges in clinopyroxene composition. The dominant rim population in the crystal separates, in rock chip mounts, and a subpopulation in the separated inclusions has the composition $X_{Mg} = 0.33$. Average rim compositions for these samples are given as "f" and "g" in Table 7. In both the inclusions and crystal separates, most crystals are homogeneous at lower Fe contents (to $X_{Mg} = 0.48$). Both the rock chip mounts and single, separated inclusions contain individually homogeneous clinopyroxene crystals with widely different compositions.

Biotite

As shown in Tables 5 and 2, the abundance of biotite in WTT samples increases with whole-rock CaO and K_2O. Biotites are rarely zoned and contain occasional apatite inclusions. Large biotite plates up to 7 cm long occur in grey pumices.

In samples 6 and 43 (Type I), biotites are rare and small, and only a single population is present ($X_{Mg} = Mg/Mg + Fe^{+2} = 0.61$ and 0.57 respectively). These values are listed in Table 8. Biotite analyses for all samples are plotted as

Table 8. Average microprobe analyses of selected biotite subpopulations

Sample	6	43	11	35T	35T
P.T.	I	I	IV	II	II
Analysis	a	b	c	d	e
SiO_2	35.95	36.82	35.89	35.66	36.50
TiO_2	4.60	4.62	4.58	4.95	3.03
Al_2O_3	14.75	14.21	14.26	14.66	16.72
V_2O_5	0.08	0.04	0.06	0.06	0.06
FeO	16.25	17.79	17.66	16.22	9.26
MnO	0.17	0.27	0.26	0.17	0.03
MgO	14.18	13.15	13.35	14.01	19.96
CaO	0.06	0.04	0.06	0.04	0.06
SrO	0.08	0.06	0.07	0.09	0.07
BaO	0.59	0.21	0.43	0.57	0.53
Na_2O	0.33	0.43	0.41	0.34	0.46
K_2O	9.41	9.38	9.60	9.86	9.72
Cl	0.03	0.04	0.02	0.04	0.02
F	0.40	0.52	0.56	0.41	0.27
H_2O*	3.80	3.75	3.70	3.78	4.00
Total	100.68	101.33	100.91	100.86	100.69
$-O \equiv Cl, F$	0.18	0.24	0.24	0.19	0.12
Total	100.50	101.09	100.67	100.65	100.57
Mg/Fe+Mg	0.609	0.569	0.574	0.606	0.793

H_2O* calculated to fill the hydroxyl site
Letters a–e correspond to analyses plotted on Fig. 7
P.T. = pumice type as in Table 2

diamonds on Fig. 7. Sample 35B (Type III) contains three compositionally distinct biotite populations both in the bulk mafic separate and in the inclusions. The most Fe-rich biotites ($X_{Mg}=0.60$) are compositionally identical to those in sample 6. The more Mg-rich populations ($X_{Mg}=0.71$ and 0.82) probably originated in the inclusions. Biotites in sample 11 (Type IV) are largely of a single composition ($X_{Mg}=0.57$) with a single more Mg-rich crystal ($X_{Mg}=0.67$). The dominant composition is listed in Table 8. In the grey (Type II) samples 35T and 13, the dominant biotite populations of the mafic separates, rock chip mounts, and inclusions are nearly identical in composition to the biotite of sample 6 ($X_{Mg}=0.61$). Homogeneous biotite crystals with higher Mg-contents (up to $X_{Mg}=0.82$) are common, particularly in the inclusions (Fig. 7). The analysis of one such Mg-biotite is given in Table 8.

Olivine

Olivine crystals were found in bulk mafic separates of samples 35B (Type III), 35T, and 13 (Type II), and large olivine crystals were separated from sample 13 during crushing. Each grain is essentially unzoned. Six crystals from 35B, two from 35T, and one from 13 are very Mg-rich ($X_{Fo}=0.89$), while seven other crystals from sample 13 are more Fe-rich ($X_{Fo}=0.84$). These values are plotted as stars on Fig. 7, and representative analyses are given in Table 7.

Titanomagnetite

Titanomagnetite is present in all WTT samples, commonly associated with clinopyroxene in small clusters. Individual titanomagnetite crystals are generally homogeneous. Ilmenite was never found.

Sample 6 (Type I) contains a single titanomagnetite population (0.7% MgO); its analysis is given in Table 9, and titanomagnetite subpopulations from all samples are plotted on an Al-Mg diagram in Fig. 8. The dominant subpopulation in sample 35B (Type III) is identical to that of sample 6 (0.7% MgO), but other, more-magnesian crystals are present in the titanomagnetite separate and in dark inclusions (1.9 and 2.0% MgO respectively). The average analysis of the inclusion population of 35B is given in Table 9. The whole-rock and glass analyses for samples 43 (Type I) and 11 (Type IV) are relatively high in Al_2O_3 compared to other WTT pumices (Table 2). Similarly, the titanomag-

Table 9. Average microprobe analyses of selected titanomagnetite subpopulations

Sample	6	43	35B	11	35T	35T	35T	13	13
P.T.	I	I	III	IV	II	II	II	II	II
Analysis	a	b	c	d	e	f	g	h	i
SiO_2	0.03	0.05	0.07	0.04	0.09	0.03	0.15	0.03	0.05
TiO_2	4.95	4.31	6.24	6.18	6.47	7.09	6.36	7.26	6.93
Al_2O_3	1.13	1.49	3.49	2.31	1.67	3.31	4.51	3.21	4.66
V_2O_5	0.29	0.47	0.58	0.51	0.37	0.53	0.47	0.54	0.72
FeO	85.00	86.64	82.52	83.97	84.37	82.23	80.88	82.17	81.06
MnO	2.10	1.42	0.59	0.91	1.51	0.70	0.63	0.69	0.35
MgO	0.68	0.59	2.11	1.25	1.14	2.13	2.77	2.09	3.03
CaO	0.00	0.01	0.08	0.03	0.04	0.01	0.02	0.02	0.02
Total	94.18	94.99	95.68	95.20	95.66	96.03	95.79	96.01	96.81
Fe_2O_3	58.11	59.27	53.97	54.88	55.40	52.85	52.81	52.58	52.33
FeO	32.71	33.31	33.95	34.58	34.52	34.67	33.36	34.85	33.97
Total	100.00	100.92	101.08	100.69	101.21	101.32	101.08	101.27	102.06

Ferric iron recalculated following Carmichael (1967); Letters a–i correspond to analyses plotted on Fig. 8
P.T. pumice type as in Table 2

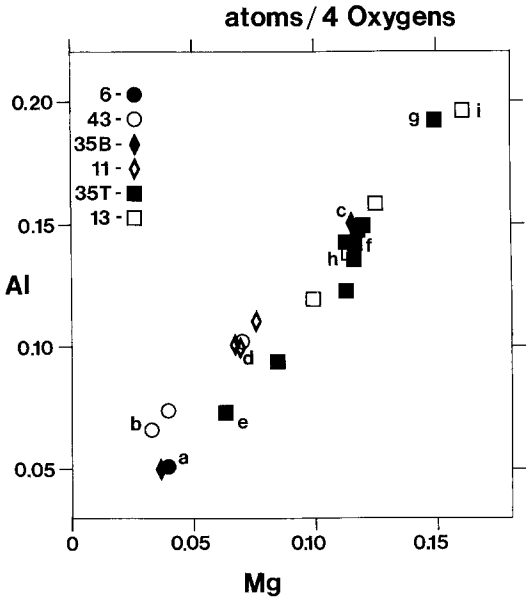

Fig. 8. Concentrations of Al and Mg atoms (per 4 oxygens) in WTT titanomagnetite subpopulations. Small letters a–i correspond to analyses listed in Table 9

netites of these two samples are displaced to higher Al_2O_3 contents compared to those from other samples (Fig. 8). Sample 43 has two titanomagnetite subpopulations, the principal one at 0.6% MgO (Table 9) and another at 1.4% MgO. Those from sample 11 are largely homogeneous at 1.3% MgO (Table 9, Fig. 8). Grey pumices 35T and 13 (Type II) contain a wide compositional range of titanomagnetites. The dominant population in each is similar (2.1% MgO; Table 9), although sample 35T also has a large subpopulation at 1.1% MgO (Table 9). Inclusions in both grey pumices contain occasional crystals with up to 3% MgO (Table 9).

Sphene

Small euhedral rhombs of sphene occur in every WTT pumice sample and in the dark inclusions. Most crystals are compositionally unzoned, although some have rims slightly richer or poorer in Ti. Type I pumices 6 and 43 have single sphene populations with 32.2 and 30.6% TiO_2 respectively (Table 10). Samples 11 (Type IV) and 35B (Type III) have two sphene populations; one is similar to those of samples 6 and 43 (<32.5% TiO_2), while the other has higher TiO_2 (>34%). Such TiO_2-rich sphenes form the dominant populations in the grey pumices 35T and 13 (34.5 and 35.7% TiO_2 respectively; Table 10), although compositions down to 32% TiO_2 are also present. As in the case of the titanomagnetites, sphenes from the Al_2O_3-rich samples 11 (Type IV) and 43 (Type I) are relatively rich in Al_2O_3. The WTT sphenes contain high contents of Zr, Nb, Y, La, Ce, and Nd. The relative concentrations of these elements in the sphenes clearly reflect whole-rock concentrations: sample 6 has both the highest whole-rock La and Ce contents and the most La-Ce-enriched sphenes. Similarly, sample 43 and its sphene are both relatively poor in Y and Ce, and rich in Zr and Nb compared to other WTT samples. Despite the high contents of trace elements in the sphenes, they account for less than 1% of the whole-rock concentrations, which reside principally in the glass (Table 2). Calculation of sphene contents in WTT samples from Ce concentration data in Tables 2 and 10 imply <0.05 wt.% sphene, consistent with modal estimates in Table 5.

Table 10. Average microprobe analyses of sphene, garnet, and amphibole

Sample	6-sp	43sp	35T-sp	13sp	43-gt	43-am
P.T.	I	I	II	II	I	I
Analysis	a	b	c	d		
SiO_2	29.21	29.49	28.50	29.55	34.46	36.38
TiO_2	32.16	30.59	34.48	35.73	3.28	1.79
ZrO_2	0.77	2.39	0.69	0.63	0.72	0.01
Nb_2O_5	0.33	0.62	0.26	0.23	0.07	0.00
V_2O_5	0.04	0.12	0.11	0.02	0.13	0.05
Y_2O_3	0.45	0.25	0.47	0.51	0.22	0.00
La_2O_3	0.64	0.43	0.34	0.36	0.01	0.00
Ce_2O_3	2.13	1.23	1.48	1.37	0.07	0.00
Nd_2O_3	0.78	0.47	0.93	0.87	0.00	0.00
Al_2O_3	1.70	2.37	1.42	1.44	6.25	14.18
FeO	2.92	3.16	1.82	1.49	20.07	23.29
MnO	0.18	0.08	0.11	0.07	1.52	1.19
MgO	0.12	0.10	0.10	0.08	0.28	5.92
CaO	25.68	26.46	25.68	26.16	31.03	11.14
SrO	0.04	0.07	0.05	0.04	0.06	0.09
BaO	0.24	0.12	0.16	0.11	0.01	0.00
Na_2O	0.08	0.07	0.11	0.08	0.11	2.22
K_2O	0.05	0.03	0.02	0.04	0.00	2.13
Cl	0.00	0.00	0.01	0.01	0.00	0.05
F	0.61	0.67	0.28	0.19	0.00	0.68
H_2O*	nc	nc	nc	nc	nc	1.59
Total	98.13	98.72	97.02	98.98	–	100.71
$-O \equiv F, Cl$	0.26	0.28	0.12	0.08	–	0.31
Total	97.87	98.44	96.90	98.90	98.29	100.40

sp = sphene; gt = garnet; am = amphibole
H_2O* calculated from stochiometry for amphiboles
nc = H_2O not calculated
P.T. = pumice type as in Table 2

Garnet and amphibole

Among other unique aspects of sample 43 (Type I), is the presence of small amounts of andradite-grossular garnet (<0.3 mm) and hastingsitic amphibole (<0.4 mm). Both phases are unzoned; in thin section, garnet is pale yellow-brown and amphibole is pleochroic in shades of greenish-brown and dark brown. Analyses of these two phases are given in Table 10. They are similar to amphiboles and garnets from monzonite and syenite nodules (Giannetti 1982) and from calc-silicate hornfelses (unpublished data) of Roccamonfina, and to garnets and amphiboles reported by Baldridge et al. (1981) for leucite-bearing lavas of the Roman Province. The garnets are unlike almandine-pyrope garnets which are occasionally found as phenocrysts in calc-alkaline volcanic rocks (Yasmasaki 1968; Green and Ringwood 1968).

Discussion

Mineralogical complexity, dark inclusions, and magma mixing

Pumices of the WTT range from crystal- and inclusion-poor white varieties, through white pumices containing grey in-

clusions, to grey varieties which themselves have darker inclusions. Sample 6, representing the dominant (Type I) white-pumice group, contains no noticeable inclusions and has the simplest mineralogy of the studied samples, with single compositional populations of all phases except clinopyroxene. All other samples have multiple populations of every phase and megascopic dark inclusions. The inclusions are texturally and mineralogically similar to the dense, grey WTT pumices (Type II), but have coarser microcrystalline groundmasses, and include more primitive crystals. Two analyzed inclusions from white-pumice hosts are more basic (Ca- and Mg-rich) than any analyzed pumices. These trachyandesite inclusions are compositionally intermediate between the WTT trachytes and subsequently erupted latites. Many WTT pumices and all separated inclusions record extreme mineralogical disequilibria, with individually homogeneous crystals of widely different compositions separated by fractions of a millimeter in the microcrystalline groundmasses.

We interpret these observations as evidence of pre-eruptive mixing involving a variety of magma types. A suggested model follows: Prior to eruption a compositionally-zoned magma chamber existed beneath Roccamonfina, with the more-evolved "white pumice" (Type I) trachytic magma overlying the "grey pumice" (Type II) trachytic magma, and the latter overlying trachyandesitic magma represented by the dark inclusions. Presumably the entire trachytic-trachyandesitic system was underlain in turn by progressively more basic magmas, which erupted after the WTT as latites, trachybasalts, and basalts. Immediately prior to or during eruption of the WTT, mixing of these various magma types appears to have occurred widely. As a result, many pumice clasts (white and grey) have megascopic to completely dissociated dark inclusions and streaks of different pumice types, similar in appearance to experimentally mixed magmas (Kouchi and Sunagawa 1982). The effects of the mixing are most evident in the more-basic WTT pumices, which characteristically contain a wide compositional spectrum of individually homogeneous crystals. With the exception of Na-rich rims on feldspars, compositional zoning within crystals is rare. This general lack of zoning suggests that juxtaposition of the diverse mineral populations was frozen-in by eruption very soon after mixing. Evidence of mixing is far more subtle in the dominant, Type I pumices, which presumably occupied the uppermost levels of the magmatic system prior to eruption. White pumices 6, 43 (Type I), and 11 (Type IV) have retained original correlations between titanomagnetite, sphene, and glass compositions, which would have been erased by extensive mixing.

Co-existence of pale-green diopside and dark-green salite crystals within a given WTT pumice sample is the most dramatic mineralogical manifestation of the inferred mixing event. Co-existing diopside and salite crystals have also been reported in a leucitite from the Alban Hills (Thompson 1977), in tephritic leucitites from Vulsini (Barton et al. 1982), in basanites and leucite-tephrites from Mts. Ernici (Civetta et al. 1981), in plutonic nodules from Roccamonfina (Giannetti 1982), and in a variety of mafic alkaline rocks from around the world (Brooks and Printzlau 1978). All of these occurrences were similarly ascribed to mixing of discrete magmas. In the Vulsini case, however, equilibrium was apparently re-established following mixing and prior to eruption, as all pyroxenes show similar rim compositions. Ghiara and Lirer (1977) and Ghiara et al. (1979) noted the presence of two clinopyroxene populations in Stage II volcanics at Roccamonfina and proposed a 2-step crystallization history involving precipitation of diopside at high pressures followed by salite at low pressure. The evidence presented in this paper, on the contrary, demonstrates that the observed subpopulations of clinopyroxene and other phases are most easily reconciled with an origin by mixing of magmas. This hypothesis is strongly supported by the relative lack of compositional zoning within grains, and the correlation of mineralogical complexity with the abundance of dark inclusions. Vollmer et al. (1981) analyzed Sr concentrations and isotopic ratios in whole-rock, groundmass, and mineral samples from four Roccamonfina specimens, including a grey (Type II) WTT pumice. They detected Sr-isotope disequilibria in all samples, which they inferred to result from widespread physical mixing of magmas containing a range of Sr-isotope ratios. Non-equilibrium mineral assemblages in plutonic nodules of Roccamonfina were interpreted by Giannetti (1982) to reflect mixing of magmas in a subvolcanic system of interlinking conduits. Cortini and Hermes (1981) presented Sr-isotope analyses of historical lavas from nearby Vesuvius showing two discrete linear decreases of $^{87}Sr/^{86}Sr$ versus time since 1750 with a discontinuity in the mid 1800's. They similarly interpreted their findings in terms of mixing between isotopically distinct magma batches. Magma mixing appears to be an important magmatic process beneath many of Italy's potassic volcanoes.

The principal purpose of undertaking detailed mineralogical investigations of WTT pumice samples was to identify pre-eruptive and pre-mixing equilibrium compositions for co-existing phases. For sample 6, this was a simple matter, as it shows little evidence of mixing and contains only a single population of all phases except clinopyroxene. For other samples this interpretation is less secure. The criteria employed were statistical dominance of subpopulations, orientations of tie-lines relative to those in sample 6 (Figs. 6 and 7), and principally, analysis of phases co-existing in small phenocryst clusters. Proposed equilibrium assemblages were confidently interpreted in this manner for three samples: 6, 43, and 35T. Only the equilibrium compositions of feldspars and sphenes in 35T are uncertain. The pre-mixing minerals of sample 35B were similar to those in 6. Mineral compositions in sample 13 are similar to those in 35T. Sample 11 appears intermediate between 6 and 35T. A key to the coexisting analyses for samples 6, 43, and 35T is given in Table 11.

Relative compositional enrichments

As shown in Fig. 4, certain pumices show strong relative enrichments in Pb, Th, Zr, Rb, Ga, Zn, and Cs compared

Table 11. Equilibrium phase assemblages

	san	plag	cpx	biot	mt	sph	glass
6	a	b	a	a	a	a	6
43	c	d	b	b	b	b	43
35T	e/g	f/h	f	d	f	c/a	35T

Letters a–h correspond to analyses in Tables 6–10. Glass analyses are in Table 2
e/g, f/h, and c/a indicate uncertainty in identifying the equilibrium subpopulation

to the main WTT trends. Many of these enriched pumices are found within the southern part of the caldera and on the high southern flank of the strato-volcano (sample 43); they have a wide range of CaO contents and include three of the four major pumice-types. Because CaO is interpreted to have increased with depth in the pre-eruptive magmatic system, the process causing these relative enrichments appears to have operated in a marginal zone, crossing other (horizontal?) compositional boundaries. Sample 43 represents the most extreme product of these enrichments. Compared to Type I pumice sample 6, 43 is also relatively enriched in Hf and U, and uniformly depleted in REE's. The garnet of sample 43 is similar to intercumulus garnets of Roccamonfina's foidal-syenite nodules, which are thought to orginate from carbonate assimilation (Giannetti 1982). We tentatively suggest that the relative enrichments in the WTT suite may also have resulted from assimilation of or reaction with carbonates near the southern edge of the magma body.

Compositional-zonation in the WTT magma: crystal fractionation

Numerous pyroclastic deposits throughout the world show trends toward progressively more-basic (Ca-rich) compositions with time (Williams 1942; Katsui 1963; Lipman 1967; Lirer et al. 1973; Hildreth 1979 and 1981), similar to the general trend of the WTT. Simple crystal settling seems unlikely to explain many compositional gradients in highly silicic magma systems (Hildreth 1981), but crystal-liquid processes may still operate in the marginal zones of silicic chambers (Michael 1983). Regardless of the controversy surrounding crystal fractionation in high-silica magmas, it is of undoubted importance in the evolution of basic to intermediate magmas, and remains one of the few quantitatively testable fractionation processes. Here we present two crystal-fractionation models for deriving a typical Type I WTT trachyte (#6) from a typical Type II composition (#35T), in an attempt to simulate the compositional diversity of the WTT prior to late-stage mixing. Several magma mixing models for the origin of inclusion-rich (Type III) pumices are also briefly discussed.

Major elements were modelled using a modification of the Wright and Doherty (1970) least-squares program. Many combinations of minerals were used in the calculations. The best fits are produced using all of the major phases: sanidine, plagioclase, clinopyroxene, biotite, titanomagnetite, and sphene. Success of the models does not depend strongly on the compositions of ferromagnesian minerals and sphene. Feldspars account for almost 90 mol% of the trachyte norms, however, and the chosen sanidine and plagioclase compositions significantly influence calculated phase proportions. Mineral analyses from sample 35T were used in the calculations. Two models are presented in Table 13; they differ only in the compositions of feldspars. Model 1 uses plagioclase (An_{87}) and sanidine (Or_{83}) core compositions, whereas model 2 uses the more sodic plagioclase (An_{54}) and sanidine (Or_{64}) rim analyses. Both models predict fractionation assemblages dominated by sanidine and plagioclase, with lesser amounts of clinopyroxene, biotite, titanomagnetite, and sphene. Model 1 has difficulty in supressing the rise of Na_2O. It calls for 48% crystallization of parental sample 35T ($\Sigma r^2 = 0.59$). Model 2, using the more sodic feldspar rim compositions calls for 85% crystallization and produces a superior major element fit ($\Sigma r^2 = 0.12$).

Table 12. Rayleigh partition coefficients used in fractionation models

	plagioclase[1, 2, 3, 4]	sanidine[1, 2]	clinopyroxene[1, 4]	biotite[1, 2, 3]	titanomagnetite[4]	sphene
Sc	0.01–0.2	0.02–0.05	7–16	12–20	2–3	0.01[a]
Cr	0.01[a]	0.01[a]	40–240	17	93–340	0.01[a]
Co	0.01[a]	0.01[a]	2–7	25	7–25	0.01[a]
Zn	0.01[a]	0.01[a]	7–12	10–20	5–13	0.01[a]
Rb	0.05–0.2	0.3–0.7	0.03	2–3	0.01[a]	0.01[a]
Sr	4	4	0.5	0.1	0.01[a]	8–21
Zr	0.01[a]	0.01[a]	0.01[a]	0.01[a]	0.01[a]	8–19
Nb	0.01[a]	0.01[a]	0.01[a]	0.01[a]	0.01[a]	63–93
Ba	0.1 –2	5–7	0.02–0.1	6–10	0.1–0.4	3–150
La	0.1 –0.7	0.07–0.12	0.1 –0.2	0.03–0.3[a]	0.2–0.4	31
Ce	0.1 –0.5	0.04–0.06	0.2 –0.7	0.03–0.3	0.1–0.4	71
Nd	0.1 –0.3	0.02–0.05	0.4 –1.3	0.03–0.3	0.2–0.5	88
Sm	0.1 –0.2	0.01–0.04	0.8 –1.8	0.06–0.3	0.3–0.5	102
Eu	0.3 –6	1.1 –4.8	0.7 –2.0	0.1 –0.2	0.2–0.4	101
Tb	0.1 –0.2	0.03–0.04	1.1 –2.0	0.1 –0.3[a]	0.4–0.7	90
Dy	0.1 –0.3	0.05–0.13	1.2 –2.6	0.1 –0.3	0.4–0.6	80
Yb	0.01–0.2	0.01–0.04	0.9 –2.0	0.2 –0.4	0.2–0.5	37
Lu	0.03–0.06	0.006	0.9 –1.8	0.2 –0.3	0.3–0.4	27
Hf	0.01–0.2	0.03–0.06	0.2 –0.3	0.01[a]	0.3–0.6	0.01[a]
Ta	0.1 –0.2	0.03–0.04	0.01[a]	0.01[a]	0.5–0.7	63–93
W	0.01[a]	0.01[a]	0.01[a]	0.01[a]	0.01[a]	0.01[a]
Th	0.01–0.2	0.01–0.03	0.01[a]	0.01[a]	0.01[a]	0.01[a]
U	0.1 –0.2	0.04	0.01[a]	0.01[a]	0.01[a]	0.01[a]

Superscripts 1–4 indicate D's taken from: 1) Arth (1976), 2) Hildreth (1977), 3) Gill (1978) and 4) Luhr and Carmichael (1980)
Sphene D's estimated from values in Tables 2 and 10 (Sr, Zr, Nb, Ba, La, Ce) and Simmons and Hedge (1978); D_{Ta} in sphene assumed equal to D_{Nb}

[a] Denotes assumed value

Table 13. Crystal-fractionation models for deriving sample 6 from 35T

Mineral weight fractions			
Phase	Model 1	Model 2	Syenite
sanidine	(e) 0.680	(g) 0.785	0.726
plagioclase	(f) 0.170	(h) 0.120	0.165
clinopyroxene	(f) 0.032	(f) 0.032	0.068
biotite	(d) 0.076	(d) 0.032	0.014
titanomagnetite	(f) 0.027	(f) 0.024	0.019
sphene	(c) 0.015	(c) 0.007	0.007
Total % xlls	47.8	85.0	

Major element calculations (wt.%)			
	6 measured	6 model 1	6 model 2
SiO_2	65.54	65.30	65.45
TiO_2	0.23	0.03	0.14
Al_2O_3	18.51	18.37	18.42
FeOt	2.14	2.00	2.07
MnO	0.21	0.18	0.26
MgO	0.29	0.14	0.23
CaO	1.20	1.26	1.20
Na_2O	4.99	5.60	5.27
K_2O	6.89	7.12	6.96
Σr^2		0.59	0.12

Trace element calculations (ppm)			
Sc[a]	0.44	1.9 –3.5	2.3–7.6
Cr[a]	3.3	0 –1.4	0
Co	1.22	1.2 –1.8	1.2–3.6
Zn	117	36 –74	57 –112
Rb	582	377–479	595 –1,177
Sr	32	120 –136	4
Zr	672	430 –477	1,385 –1,582
Nb	39	19 –26	48–71
Ba	<6	3 –49	0–1
La	154	111 –124	276 –354
Ce	266	155 –168	354 –427
Nd	50	53 –57	116 –137
Sm[a]	7.11	7.9 –8.4	16.5–19.2
Eu	0.8	0.1 –1.2	0 –0.9
Tb[a]	0.73	1.3 –1.4	2.8–3.2
Dy	5.74	5.4 –5.9	10.4–13.8
Yb	5.34	4.0 –4.3	10.3–12.2
Lu	0.71	0.55–0.56	1.57–1.69
Hf	15.2	12.0–12.5	37 –41
Ta	1.35	1.15–1.59	2.67–4.13
W	13.8	9.5	33
Th	75.3	53 –54	171 –184
U	17.0	10.9	35 –36

Small letters a–h correspond to mineral analyses in Tables 6–11
Syenite represents the average of syenites PC13 and SPo from Giannetti (1982), converted to weight fractions neglecting apatite and secondary hornblende

[a] Indicates that the observed concentration in sample 6 is not bracketed by the two models combined

Trace element concentrations for sample 6 were predicted from the phase proportions given in the major-element models, and the ranges of partition coefficients (D_i's) listed in Table 12, assuming Rayleigh fractionation (Arth 1976). D_i's appropriate to the studied trachytes are not available in the literature. In order to preform the fractionation calculations, it was necessary to include D_i's from a wide spectrum of natural samples, including high-silica rhyolites (Hildreth 1977), particularly for sanidine and biotite. The calculations predict a wide range of abundances for each trace element (Table 13), as a consequence of the large differences in the total separated crystal content predicted by the major-element models (48–85%) and uncertainties in partition coefficients (Table 12). In most cases, the wide elemental ranges predicted by the two models bracket the analyzed values for sample 6. Predicted concentrations of Sc and Cr are slightly low. Of the rare earth elements, only Sm and Tb concentrations are not within the predicted ranges. The general success of the trace-element modelling is primarily a measure of the large uncertainties in the compositions of fractionating feldspars and in partition coefficients. Only a single set of REE partition coefficients for sphene is available in the literature (Simmons and Hedge 1978), for instance, but the high D_i's in sphene for many trace elements make these values critical to the calculations. Until the ambiguities in partition coefficients are significantly reduced, geochemical models can not hope to realistically discriminate crystal fractionation from other, perhaps concurrent, magma chamber processes.

Probably the strongest supportive evidence for crystal-fractionation in the WTT magmas comes from the cumulate inclusions brought to the surface by Roccamonfina's pyroclastic eruptions. Cumulate syenite nodules represent a relatively common inclusion type, accounting for about 6% of the inclusions in an extensive suite (Giannetti 1982). These syenites contain sanidine, plagioclase, clinopyroxene, biotite, titanomagnetite, sphene, apatite, and secondary hornblende, and closely match the calculated fractionation assemblages (Table 13) in the nature, proportions, and compositions of phases. A combined mode for the syenites, converted to weight fractions, is given for comparison in Table 13. Sanidine-dominated crystal clusters, occurring within large vesicles of WTT pumices, may represent syenite fragments settling through the magma or torn from the chamber walls, which acted as gas nucleation sites on eruption. If the Type I trachytes of the WTT did evolve from Type II magmas through 50–85% syenite fractionation, the estimated volume of Type I magma (4–7 km^3) implies 4–40 km^3 of syenite cumulates beneath Roccamonfina from the last fractionation step of Stage II alone.

Several major and trace element magma-mixing models were also calculated in order to test an origin for the inclusion-rich (Type III) sample #35B through combination of Type I pumice #6 and either Type II pumice #35T or the dark inclusion 100inc. These two models were relatively successful ($\Sigma r^2 = 0.43$ and 0.33 respectively) calling for 18.9 wt.% of 35T or 12.5 wt.% of 100inc, and closely matching the trace element data for 35B (Table 2). Magma mixing and crystal fractionation may be particularly important processes at Roccamonfina and other Italian volcanoes owing to the relatively low viscosities of potassic magmas compared to more common calc-alkaline types.

Acknowledgements. We are indebted to Warren Sharp for kindly performing K-Ar dating of the WTT, to Frank Asaro and Helen

Michel for INA analyses, and to the Carabinieri of Teano who gave B.G. "lodging" while investigating two terrorists during the summer of 1978. Reviews by Ian Carmichael, J.C. Eichelberger, Gail Mahood, and R.N. Thompson led to significant improvements in the manuscript. J.L. was supported by NSF EAR 78-03642 (Carmichael) while B.G., being refused funding from CNR (Comitato 05), supported this research with his high school teaching salary.

References

Appleton JD (1972) Petrogenesis of potassium-rich lavas from the Roccamonfina Volcano, Roman Region, Italy: J Petrol 13 3:425–456

Arth JG (1976) Behavior of trace elements during magmatic processes – A summary of theoretical models and their applications: US Geol Surv Res 4, 1:41–47

Baldridge WS, Carmichael ISE, Albee AL (1981) Crystallization paths of leucite-bearing lavas: Examples from Italy: Contrib Mineral Petrol 76:321–335

Barberi F, Innocenti F, Lirer L, Munno R, Pescatore T, Santacroce R (1978) The Campanian Ignimbrite: a major prehistoric eruption in the Neapolitan area (Italy): Bull Volcanol 41:1–22

Barton M, Varekamp JC, Van Bergen MJ (1982) Complex zoning of clinopyroxenes in the lavas of Vulsini, Latium, Italy: Evidence for magma mixing: J Volcanol Geoth Res 14:361–388

Brooks CK, Printzlau I (1978) Magma mixing in mafic alkaline volcanic rocks: The evidence from relict phenocryst phases and other inclusions: Jour Volcanol Geoth Res 4:315–331

Carmichael ISE (1967) The iron-titanium oxides of salic volcanic rocks and their associated ferromagnesian silicates: Contrib Mineral Petrol 14:36–64

Carter SR, Evensen NM, Hamilton PJ, O'Nions RK (1978) Continental volcanics derived from enriched and depleted source regions: Nd- and Sr-isotope evidence: Earth and Planet Sci Lett 37:401–408

Civetta L, Innocenti F, Manetti P, Peccerillo A, Poli G (1981) Geochemical characteristics of potassic volcanics from Mts. Ernici (Southern Latium, Italy): Contrib Mineral Petrol 78:37–47

Clough BJ, Wright JV, Walker GPL (1981) An unusual bed of giant pumice in Mexico: Nature 289:49–50

Cornell WC, Sigurdsson H, Sparks RSJ (1979) The Campanian Ignimbrite of SW Italy: Eruptive phases and variations in glass chemistry: Trans Am Geophys Soc EOS 60, no 18, 409

Cortini M, Hermes OD (1981) Sr isotopic evidence for a multisource origin of the potassic magmas in the Neapolitan area (S. Italy): Contrib Mineral Petrol 77:47–55

Cortini M, Roberti N, Scandone R (1975) Geocronologia e paleomagnetismo del vulcano di Roccamonfina: Ann Geof 28:129–138

Cox KG, Hawkesworth CJ, O'Nions RK, Appleton JD (1976) Isotopic evidence for the derivation of some Roman Region volcanics from anomalously enriched mantle: Contrib Mineral Petrol 56:173–180

Devoto G (1965) Lacustrine Pleistocene in the lower Liri Valley (Southern Latium): Geologica Romana IV, 291–368

Di Girolamo P (1970) Differenziazione gravitativa e curve isochimiche nella ignimbrite Campana: Rand Soc It Min e Petr 26-2:547–588

Di Girolamo P, Keller J (1972) Zur Stellung des grauen Campanichen Tuffs, innerhalb des quartären Vulkanismus Campaniens (Sud Italien): Ber Natur Ges Freiburg 61–62:85–92

Drake MJ, Weill DF (1972) New rare earth element standards for electron microprobe analysis: Chem Geol 10:179

Falchi G, Tonani F (1974) Procedure rapide per l'analisi delle rocce: CNEN RT/GEO 64, 6, Roma

Fisher RV (1979) Models for pyroclastic surges and pyroclastic flows: J Volcanol Geoth Res 6:305–318

Ghiara MR, Lirer L, Stanzione L (1973) Contributo alla conoscenza vulcanologica e petrografica del vulcano di Roccamonfina: Per Min 42:267–293

Ghiara MR, Lirer L (1977) Mineralogy and geochemistry of the "low potassium" series of the Roccamonfina volcanic suite (Campania, South Italy): Bull Volcanol 41:39–56

Ghiara MR, Lirer L, Munno R (1979) Mineralogy and geochemistry of the "Low-potassium series" of the Campania volcanics (South Italy): Chemical Geology 26:29–49

Giannetti B (1979) The geology of Roccamonfina caldera (Campanian Province, Italy): Giornale Geologia ser 2:43:187–206

Giannetti B (1982) Cumulate inclusions from K-rich magmas, Roccamonfina volcano, Italy: Earth and Planet Sci Lett 57:313–335

Giannetti B, Nicoletti M, Petrucciani C (1979) Datazioni K-Ar di lave leucitiche dello strato-vulcano di Roccamonfina: Rend Soc It Mineral Petr 35:349–354

Gill JB (1978) Role of trace element partition coefficients in models of andesite genesis: Geochim Cosmochim Acta 42:709–724

Green TH, Ringwood AE (1968) Origin of garnet phenocrysts in calc-alkaline rocks: Contrib Mineral Petrol 18:163–174

Hawkesworth CJ, Vollmer R (1979) Crustal contamination versus enriched mantle: $^{143}Nd/^{144}Nd$ and $^{87}Sr/^{86}Sr$ evidence from the Italian volcanics: Contrib Mineral Petrol 69:151–165

Hildreth W (1977) The magma chamber of the Bishop Tuff: Gradients in temperature, pressure, and composition: Univ Calif Berkeley Unpubl Ph D dissert, 328 p

Hildreth W (1979) The Bishop Tuff: Evidence for the origin of compositional zonation in silicic magma chambers: Geol Soc Am Spec Paper 180:43–75

Hildreth W (1981) Gradients in silicic magma chambers: Implications for lithospheric magmatism: J Geophys Res 86, B11:10153–10192

Katsui Y (1963) Evolution and magmatic history of some Krakatoan calderas in Hokkaido, Japan: Jour Fac Sci, Hokkaido Univ, ser 4:11:631–650

Kouchi A, Sunagawa I (1982) Experimental study of mixing of basaltic and dacitic magmas: Tohoku Univ Sci Reports ser III, XV, no 2, 163–175

Lipman PW (1967) Mineral and chemical variations within an ash-flow sheet from Aso caldera, southwestern Japan: Contrib Mineral Petrol 16:300–327

Lirer L, Pescatore T, Booth B, Walker GPL (1973) Two Plinian pumice-fall deposits from Somma-Vesuvius, Italy: Geol Soc Am Bull 84:759–772

Long PE (1978) Experimental determination of partition coefficients for Rb, Sr, and Ba between alkali feldspar and silicate liquid: Geochim Cosmochim Acta 42:833–846

Luhr JF, Carmichael ISE (1980) The Colima volcanic complex: I. Post-caldera andesites from Volcan Colima: Contrib Mineral Petrol 71:343–372

Mahood GA (1980) Geological evolution of a Pleistocene rhyolitic center – Sierra La Primavera, Jalisco, Mexico: J Volcanol Geoth Res 8:199–230

Masuda A, Nakamura N, Tanaka T (1973) Fine structures of mutually normalized rare-earth patterns of chondrites: Geochim Cosmochim Acta 37:239–248

Michael PJ (1983) Chemical differentiation of the Bishop Tuff and other high-silica magmas through crystallization processes: Geology 11:31–34

Perlman I, Asaro F (1969) Pottery analysis by neutron activation: Archaeometry 11:21–52

Simmons EC, Hedge CE (1978) Minor-element and Sr-isotope geochemistry of Tertiary stocks, Colorado Mineral Belt: Contrib Mineral Petrol 67:379–396

Sparks RSJ, Self S, Walker GPL (1973) Products of ignimbrite eruptions: Geology, Nov 115–118

Taylor Jr, HP, Giannetti B, Turi B (1979) Oxygen isotope geochemistry of the potassic igneous rocks from the Roccamonfina volcano, Roman Comagmatic Region, Italy: Earth and Planet. Sci Lett 46:81–106

Thompson RN (1977) Primary basalts and magma genesis – III. Alban Hills, Roman Comagmatic Province, Central Italy: Contrib Mineral Petrol 60:91–108

Varekamp JC (1980) The geology of the Vulsinian area, Lazio, Italy: Bull Volcanol 43–3:487–503

Vollmer R, Hawkesworth CJ (1980) Lead isotopic composition of the potassic rocks from Roccamonfina (South Italy): Earth Planet Sci Lett 47:91–101

Vollmer R, Johnston K, Ghiara MR, Lirer L, Munno R (1981) Sr isotope geochemistry of megacrysts from continental rift and converging plate margin alkaline volcanism in south Italy: J Volcanol Geoth Res 11:317–327

Williams H (1942) The geology of Crater Lake National Park, Oregon, with a reconnaissance of the Cascade Range southward to Mount Shasta: Carnegie Inst Washington Publ 540:162 p

Wright TL, Doherty PC (1970) A linear programming and least squares computer method for solving petrologic mixing problems: Geol Soc Am Bull 81:1995–2008

Yamasaki M (1958) Notes on rock-forming minerals – 2. Garnets from volcanic rocks: J Geol Soc Jpn 64, no 758:601–604

Received January 1, 1983; Accepted August 8, 1983